Nano Research

Open Access

Research Article

Single-atom Pd confined in Ti_3C_2 nanosheet for boosted room-temperature trace NO_2 monitoring

Yang Cai, Jinlong Xiong, Yuwei Wang, Hafiz Muhammad Adeel Sharif, Jiahao Cai, Ting Pan, Xueren Tan, Zhuo Li, and Changping Li ✉

Research Center for Eco-Environmental Engineering, Dongguan University of Technology, Dongguan 523808, China

Cite this article: *Nano Research*, **2025**, *18*, 94907285. https://doi.org/10.26599/NR.2025.94907285

ABSTRACT: Two-dimensional MXenes have great potential for gas sensing applications due to their distinct electronic structure and unique surface properties. However, low sensitivity and poor selectivity to target gas at room temperature are major shortcomings of MXene materials. In this study, $PdCl_2$ was used to decorate Pd single atoms (Pd_{SA}) on Ti_3C_2 nanosheet (Ti_3C_2/Pd_{SA}). The Pd^{2+} was directly reduced (*in-situ*) into a Pd_{SA} due to abundant Ti vacancies and the inherent reducing ability of Ti_3C_2 MXene. The Ti_3C_2/Pd_{SA} sensor exhibited the highest response of 0.289 to 1 ppm NO_2, which is 28.9 and 7.8 times higher over pristine Ti_3C_2 and Pd nanoparticles (Pd_{nano})-decorated on Ti_3C_2 (Ti_3C_2/Pd_{nano}), respectively. Simultaneously, the Ti_3C_2/Pd_{SA} sensor possessed an ultralow detection limit (10 ppb) and excellent selectivity towards NO_2. The enhanced gas sensing mechanism of Ti_3C_2/Pd_{SA} was investigated in detail through the activation energy calculation, *in-situ* diffuse reflectance infrared Fourier transform spectroscopy (DRIFTS), and density functional theory (DFT) studies. The rich active sites, chemical sensitization effect, and NO_2 adsorption enhancement resulting from the Pd single atoms in Ti_3C_2/Pd_{SA} significantly boosted sensing performance. This work can provide new insights and guidelines for fabricating highly effective NO_2 sensors operated at room temperature.

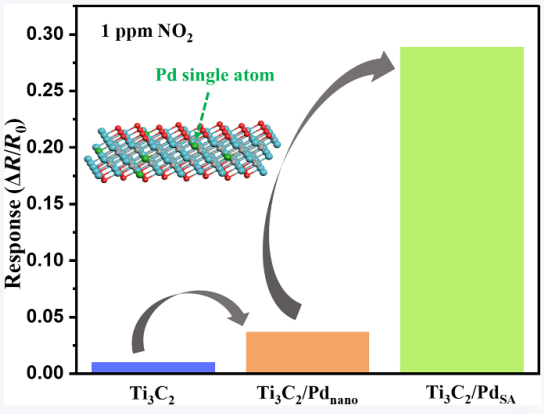

KEYWORDS: NO_2 sensor, Pd single atom, Ti_3C_2 MXene, sensing mechanism, *in-situ* diffuse reflectance infrared Fourier transform spectroscopy (DRIFTS)

1 Introduction

Air pollution requires serious attention due to rapid development of transportation and industry. Among air pollutants, nitrogen dioxide (NO_2) is a typical toxic gas mainly resulting from automotive emissions and fossil fuel combustion. It causes serious diseases, even if the human body is exposed to the part per billion (ppb) level, and contributes to acid rain [1, 2]. Hence, the effective detection of NO_2 is of great significance to ensure human and environmental safety. Gas sensors have been a promising strategy for monitoring NO_2, and the design of sensing material is the core of NO_2 gas sensors [3]. In particular, the development of NO_2 sensing materials with high sensitivity, good selectivity, and low detection limit for real-time NO_2 monitoring at room temperature is urgent and crucial at present.

Received: November 13, 2024; **Revised:** January 7, 2025
Accepted: February 6, 2025

✉Address correspondence to licpbit@hotmail.com

Currently, diverse two-dimensional (2D) materials, including graphene [4], transition metal dichalcogenides [5, 6], conductive metal-organic frameworks (MOFs) [7, 8], and MXenes [9–11], have been reported as sensing materials for room-temperature NO_2 detection. Among them, MXenes have already shown the great potential to fabricate high-quality gas sensors due to their superior metallic conductivity, plentiful surface terminals, and large specific surface area [12–16]. However, the pure MXenes exhibited weak response and poor selectivity toward NO_2 gas at room temperature, limiting their wide application for accurately detecting NO_2. The composition of MXenes with metal oxide semiconductors (such as Ti_3C_2/TiO_2 [3, 17], Ti_3C_2/TiO_2/reduced graphene oxide (rGO) [18], Ti_3C_2/SnO_2 [19, 20], and Ti_3C_2/ZnO [21]) or metal nanoparticles (NPs) (such as Ti_3C_2/Au NPs [22], Ti_3C_2/Pt NPs [22, 23], and Ti_3C_2/TiO_2/Au NPs [24]) is a general strategy to enhance their sensing performance.

Single-atom catalysts (SACs) have recently attracted a considerable attention owing to the high metal atom utilization and numerous unsaturated configurations of active centers [25–27]. For gas sensor application, the unsaturated metal center not only results

in the potential activation of target gas molecules but can also induce more electron transfer [28, 29]. Previous studies have preliminarily demonstrated the tremendous potential of SACs for gas sensors by designing SACs-functionalized metal oxides [30–32]. A novel step-rich ZnO ladder decorated by Au SACs (Au_1-ZnO) was designed for NO_2 detection, which exhibited a 1.6-fold higher response compared to Au NP-ZnO [33]. In general, noble metals (Pd, Pt, Au, etc.) have been applied as sensitization catalysts to improve the sensing properties of metal oxides. Among these noble metals, Pd can adsorb numerous O_2 molecules to dissociate into active oxygen species through the spillover effect and reduce the activation energy during gas sensing process [34]. Thus, MXenes functionalized by the Pd SACs are expected to improve the room-temperature NO_2 sensing performance of pristine MXenes. To the authors' knowledge, limited work has been carried out on the SACs-functionalized MXenes sensing materials for room-temperature NO_2 detection. Besides, the enhancement sensing mechanism resulting from the introduced SACs needs to be deeply explored and revealed.

In this work, Ti_3C_2 MXene nanosheets offer numerous active sites (due to their vacancies and ultrathin nanosheet structure) that tightly hold Pd atoms. The available Ti vacancies and reducing ability of Ti_3C_2 MXene endorsed and stabilized Pd^{2+} to Pd single atom (Pd_{SA}) and the resulting composite Ti_3C_2/Pd_{SA} used for NO_2 sensing at room temperature (Fig. 1). Moreover, the pristine Ti_3C_2 and Pd nanoparticles (Pd_{nano})-decorated Ti_3C_2 (Ti_3C_2/Pd_{nano}) were prepared and then applied for NO_2 sensing properties. The Ti_3C_2/Pd_{SA} sensor exhibited high response, ultralow detection limit, and good selectivity to NO_2 at room temperature, significantly exceeding the sensing performance of pristine Ti_3C_2 and Ti_3C_2/Pd_{nano}. The enhancement sensing mechanism of Pd SACs in Ti_3C_2/Pd_{SA} was thoroughly discussed through activation energy calculation, *in-situ* diffuse reflectance infrared Fourier transform spectroscopy (DRIFTS), and density functional theory (DFT) studies. This work expands the SACs application in gas sensors and provides a new strategy to design high-efficiency MXene-based sensing materials for NO_2 monitoring at very low concentrations.

2 Experimental

2.1 Fabrication of Ti_3C_2 nanosheet, Ti_3C_2/Pd_{SA}, and Ti_3C_2/Pd_{nano} gas sensors

The Ti_3C_2 MXene nanosheet was synthesized according to our previous work [35]. To prepare the Ti_3C_2/Pd_{SA}, $PdCl_2$ (10 mg) was added to ultrapure water (100 μL), and then ultrasonication was performed for 10 min. After ultrasonic treatment, 20 μL $PdCl_2$ dispersion was immediately added to ultrapure water (100 mL). This solution was sonicated for 1 h and then slowly dropped into Ti_3C_2 nanosheet dispersion (60 mL, 4.0 mg·mL^{-1}) under vigorous stirring. The reaction mixture was stirred for 8 h. The mixture was then washed, freeze-dried, and further treated in H_2/Ar atmosphere at 200 °C for 2 h to obtain Ti_3C_2/Pd_{SA}. To prepare the Ti_3C_2/Pd_{nano}, the $PdCl_2$ (20 mg) was added to Ti_3C_2 nanosheet dispersion (60 mL, 4.0 mg·mL^{-1}) under stirring for 0.5 h. The formic acid (5 mL) was added to the above mixture under stirring for 1 h. The mixture was then washed, freeze-dried, and further treated in H_2/Ar atmosphere at 200 °C for 2 h to obtain Ti_3C_2/Pd_{nano}. 5 mg of Ti_3C_2, Ti_3C_2/Pd_{nano}, and Ti_3C_2/Pd_{SA} were independently ultrasonic-dispersed in 1 mL ultrapure water. The dispersion of each material was deposited on the ceramic substrate with interdigitated Au electrodes using a spin coating method. After drying in ambient conditions, Ti_3C_2, Ti_3C_2/Pd_{nano}, and Ti_3C_2/Pd_{SA} gas sensors were obtained.

2.2 Characterization and gas sensing measurements

The surface morphology and microstructure of materials were characterized by scanning electron microscopy (SEM, Zeiss Sigma300), transmission electron microscopy (TEM, JEOL F200), and the aberration-corrected scanning TEM in high-angle annular dark-field (AC-STEM-HAADF, Spectra 300). The crystal structure of materials was carried out by X-ray diffraction (XRD, Ultima IV) with a Cu Kα radiation source. The surface element states of materials were analyzed using X-ray photoelectron spectroscopy (XPS, ESCALAB250). To investigate the sensing mechanism, *in-situ* DRIFTS measurements were carried out using the Bruker INVENIO S FTIR spectrometer, which was equipped with an *in-situ* diffuse-reflectance reaction chamber. All gas sensing experiments of the sensors were performed on a homo-made measurement system (Fig. S1 in the Electronic Supplementary Material (ESM)). An electrochemical workstation (CHI 760E, CH Instruments Inc.) was used to record the real-time current of the sensors at a fixed voltage of 1 V. The mass flow controllers (D07-19B, Beijing Sevenstar Flow Co., Ltd.) were used to regulate gas flow rates for different concentrations of target gas. Different humidity conditions were produced by bubbling dry air through a water bubbler jar and monitored by the commercial hygrometer. Gas sensing measurements were performed at room temperature of 24 °C and dry air except for the humidity effect experiments. The response value of the sensor was calculated using the following equation

$$\text{Response} = (R_g - R_0)/R_0 \quad (1)$$

where R_g is the resistance in the tested gas, and R_0 is the resistance in dry air.

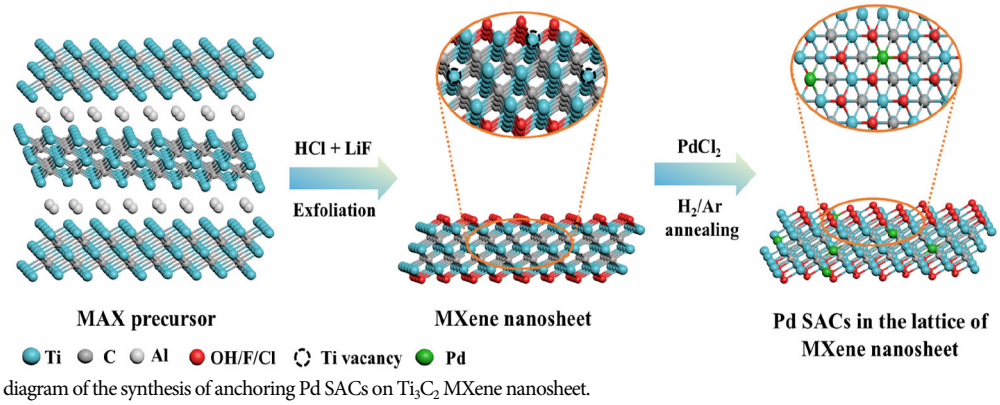

Figure 1 Schematic diagram of the synthesis of anchoring Pd SACs on Ti_3C_2 MXene nanosheet.

2.3 Calculation method

Density functional theory calculations were carried out through the Vienna *ab Initio* package (VASP), with Perdew–Burke–Ernzerhof (PBE) formulation for generalized gradient approximation (GGA). The projected augmented wave (PAW) potentials with a kinetic energy cutoff of 400 eV were adopted. The dispersion interactions were described using Grimme's DFT-D3 methodology. The structure optimization used the force convergence criterion of 0.02 eV·Å^{-1}. The equilibrium lattice constants of hexagonal Ti_3C_2 monolayer unit cell in a Z direction vacuum of 25 Å were optimized to be a = 3.026 Å, a = 3.018 Å, a = 3.060 Å, and then used to build a 4 × 4 supercell in the X and Y directions. The Brillouin zone was sampled through a 2 × 2 × 1 k-point grid during the optimization of the structure. The adsorption energy (E_{ad}) of gas on the surface of sensing material was computed as

$$E_{ad} = E_{surf/gas} - E_{surf} - E_{gas} \quad (2)$$

where $E_{surf/gas}$, E_{surf}, and E_{gas} represent the total surface energy of the adsorbed gas molecule, the clean surface, and the isolated gas molecule, respectively.

3 Results and discussion

3.1 Materials characterization

The SEM and TEM measurements were used to investigate the morphology of Ti_3C_2 nanosheet, Ti_3C_2/Pd_{nano}, and Ti_3C_2/Pd_{SA}. The ultrathin Ti_3C_2 nanosheet (Fig. S2(a) in the ESM and Fig. 2(a)) was prepared using the liquid phase exfoliation method with hydrochloric acid/lithium fluoride. During the etching process on the parent MAX (Ti_3AlC_2), numerous Ti vacancies were formed on the surface of Ti_3C_2, resulting from some Ti atoms being ripped off (see the HAADF-STEM image in Fig. S2(d) in the ESM). Due to its ability to trap alien atoms and excellent reducing capacity, the obtained Ti_3C_2 nanosheet is perfectly suitable for anchoring single atoms [36]. The typical SEM and TEM images (Fig. S2(c) in the ESM and Fig. 2(d)) of Ti_3C_2/Pd_{SA} exhibit that it still retained the ultrathin nanosheet morphology. The high-resolution TEM image (Fig. 2(e)) of Ti_3C_2/Pd_{SA} shows a lattice spacing of 0.26 nm, attributing to the (106) plane of Ti_3C_2. The HAADF-STEM image (Fig. 2(f)) of Ti_3C_2/Pd_{SA} displays that the single Pd atom sparklets (marked by red circles) disperse over the surface of Ti_3C_2 support without agglomerate. In addition, the Ti_3C_2 nanosheet anchored with Pd nanoparticles sample was also prepared using a similar method for comparison. The SEM and TEM images (Fig. S2(b) in the ESM and Figs. 2(b) and 2(c)) of Ti_3C_2/Pd_{nano} show that Pd nanoparticles were uniformly distributed on the surface of Ti_3C_2. The energy dispersive spectroscopy (EDS) elemental mapping images of Ti, C, and Pd of Ti_3C_2/Pd_{nano} and Ti_3C_2/Pd_{SA} are shown in Figs. 2(g) and 2(h). The Pd present in Ti_3C_2/Pd_{SA} displayed much weaker signals than that of Ti_3C_2/Pd_{nano} and uniformly dispersed on the Ti_3C_2 nanosheet, which is consistent with the Pd single atom structure.

The powder X-ray diffraction was performed to characterize the structure of the Ti_3C_2 nanosheet, Ti_3C_2/Pd_{nano}, and Ti_3C_2/Pd_{SA}. In Fig. 3(a), the characteristic peaks at 8.1°, 17.1°, 21.5°, 25.4°, and 35.1° are corresponding to the (002), (004), (006), (008), and (010) crystal planes of Ti_3C_2 nanosheet, respectively [37]. After being anchored with Pd nanoparticles, the characteristic peaks at 40.1° and 46.8° represented the (111) and (200) planes of Pd (PDF #46-1043) were observed [7]. Simultaneously, the characteristic peak (002) of Ti_3C_2 nanosheet in Ti_3C_2/Pd_{nano} moved from 7.9° to 5.7° due to the increase of interlayer spacing between Ti_3C_2 nanosheet, indicating that Pd nanoparticles interleaved Ti_3C_2 nanosheets. For the XRD pattern of Ti_3C_2/Pd_{SA}, no characteristic peaks of Pd nanoparticles appeared, and the distinctive peaks of Ti_3C_2 did not change significantly. These results suggested that the decoration of Pd atoms did not considerably alter the crystal structure of Ti_3C_2.

The FTIR and XPS spectra were carried out to analyze the chemical structure and the surface electronic properties of Ti_3C_2/Pd_{nano} and Ti_3C_2/Pd_{SA}. As shown in Fig. 3(b), the Pd 3d XPS spectrum of Ti_3C_2/Pd_{nano} displays the two characteristics peaks at 335.08 eV for Pd^0 $3d_{5/2}$ and 340.28 eV for Pd_0 $3d_{3/2}$ with an energy

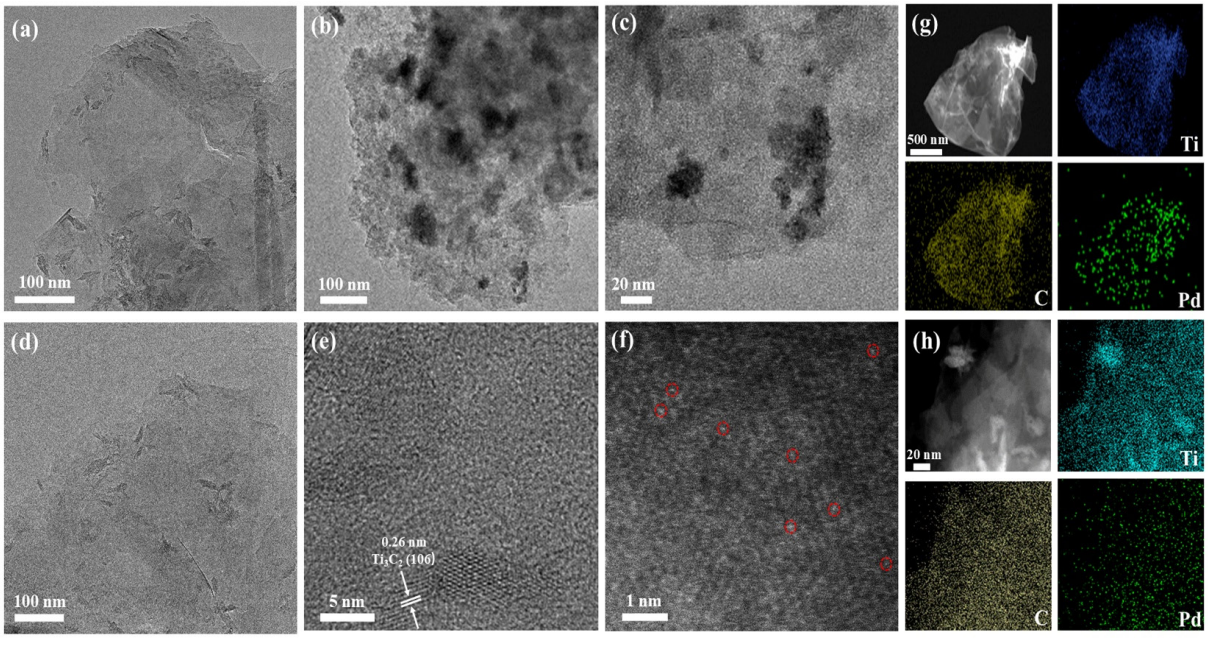

Figure 2 ((a)–(e)) TEM images of (a) Ti_3C_2 nanosheet, ((b) and (c)) Ti_3C_2/Pd_{nano}, and ((d) and (e)) Ti_3C_2/Pd_{SA}; (f) AC-STEM-HAADF image of Ti_3C_2/Pd_{SA}; and ((g) and (h)) STEM images and the corresponding EDS images of (g) Ti_3C_2/Pd_{nano} and (h) Ti_3C_2/Pd_{SA}.

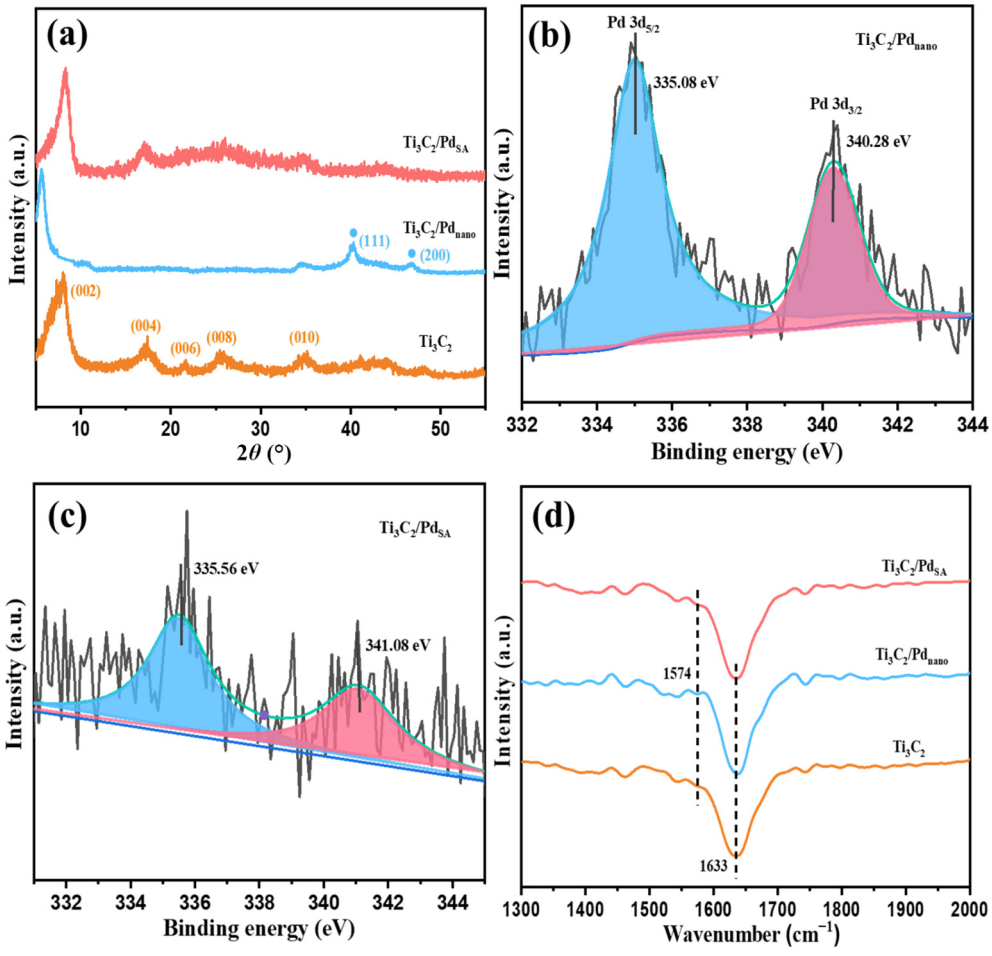

Figure 3 (a) XRD patterns of Ti_3C_2 nanosheet, Ti_3C_2/Pd_{nano}, and Ti_3C_2/Pd_{SA}; ((b) and (c)) Pd 3d XPS spectra of (b) Ti_3C_2/Pd_{nano} and (c) Ti_3C_2/Pd_{SA}; and (d) FTIR spectra of Ti_3C_2 nanosheet, Ti_3C_2/Pd_{nano}, and Ti_3C_2/Pd_{SA}.

gap of 5.2 eV, which were identified as the metallic palladium (Pd^0) [7]. For Ti_3C_2/Pd_{SA} (Fig. 3(c)), two centered peaks at 335.56 and 341.08 eV were found (the feature at 336.9 and 342.2 eV, typical for the Pd^{2+} state [38]). Therefore, the Pd 3d peaks of Ti_3C_2/Pd_{SA} located between the Pd^0 and Pd^{2+} typical peak positions, suggesting that the valent state of the Pd atom was between 0 and +2 [38]. In Fig. 3(d), the vibration peak of Ti_3C_2 at 1633 cm^{-1}, corresponding to the bending vibration of the –OH group [37], was found in these three samples. A new peak at 1574 cm^{-1} of Ti_3C_2/Pd_{nano}, associated with the vibration of adsorbed H_2O on metal nanoparticles, demonstrates the presence of Pd nanoparticles [7]. This new peak was not found in the FTIR spectrum of Ti_3C_2/Pd_{SA}, similar to pristine Ti_3C_2. These results again confirmed that Pd atoms were atomically dispersed in Ti_3C_2/Pd_{SA}, which was in good agreement with HAADF-STEM and XRD results.

3.2 NO_2 sensing characteristics

The sensing performance of the Ti_3C_2 nanosheet, Ti_3C_2/Pd_{nano}, and Ti_3C_2/Pd_{SA} sensors were investigated at room temperature. Firstly, the gas-sensing selectivity of these three sensors was examined. The response of the sensors to 1 ppm NO_2 and 100 ppm other typical interfering gases (NH_3, NO, CO, CO_2, toluene, acetone, trimethylamine, and ethanol) were measured, as shown in Figs. 4(a) and 4(b). The results showed that the sensing response of Ti_3C_2 increased in all analytes after being decorated with Pd nanoparticles or atoms. Among these interfering gases, response values of Ti_3C_2/Pd_{nano} and Ti_3C_2/Pd_{SA} to 100 ppm toluene significantly increased to 0.130 and 0.141. For 1 ppm NO_2, response values of Ti_3C_2/Pd_{nano} and Ti_3C_2/Pd_{SA} were raised to 0.037 and 0.289, which were 3.7 and 28.9 times higher than that of pristine Ti_3C_2. These comparisons indicated the excellent NO_2 selectivity of Ti_3C_2/Pd_{SA}. Meanwhile, the decoration of Pd atoms can effectively enhance the NO_2 response of Ti_3C_2. Then, the dynamic response of the sensors to 1–20 ppm NO_2 was measured. In Fig. 4(c), it can be clearly seen that Ti_3C_2/Pd_{SA} displayed the highest response (0.286–0.818) to 1–20 ppm NO_2 among these three sensors. The response of these sensors increased upon increasing NO_2 concentration (Fig. 4(d)). The Ti_3C_2/Pd_{SA} (R^2 = 0.9536) exhibited a better linear relationship between the response and NO_2 concentration than Ti_3C_2/Pd_{nano} (R^2 = 0.8901) and pure Ti_3C_2 (R^2 = 0.7679). In addition, the sensitivity of Ti_3C_2/Pd_{SA} and Ti_3C_2/Pd_{nano} were 0.0268 and 0.0110 ppm^{-1}, respectively, which were 134 and 55 times of pure Ti_3C_2 (0.0002 ppm^{-1}) [39]. The lowest detection limits of Ti_3C_2/Pd_{SA} and Ti_3C_2/Pd_{nano} were 10 and 50 ppb, respectively, whereas Ti_3C_2 cannot detect NO_2 below 200 ppb (Fig. S3 in the ESM). These results demonstrated that the Pd atoms decoration could effectively improve the sensing performance of pure Ti_3C_2 to NO_2, which also displayed a more substantial promotion effect than that of Pd nanoparticles. The reproducibility of these sensors was also measured by responding to 1 ppm NO_2 during 5 consecutive test cycles, as shown in Fig. 4(e). The corresponding resistance changes

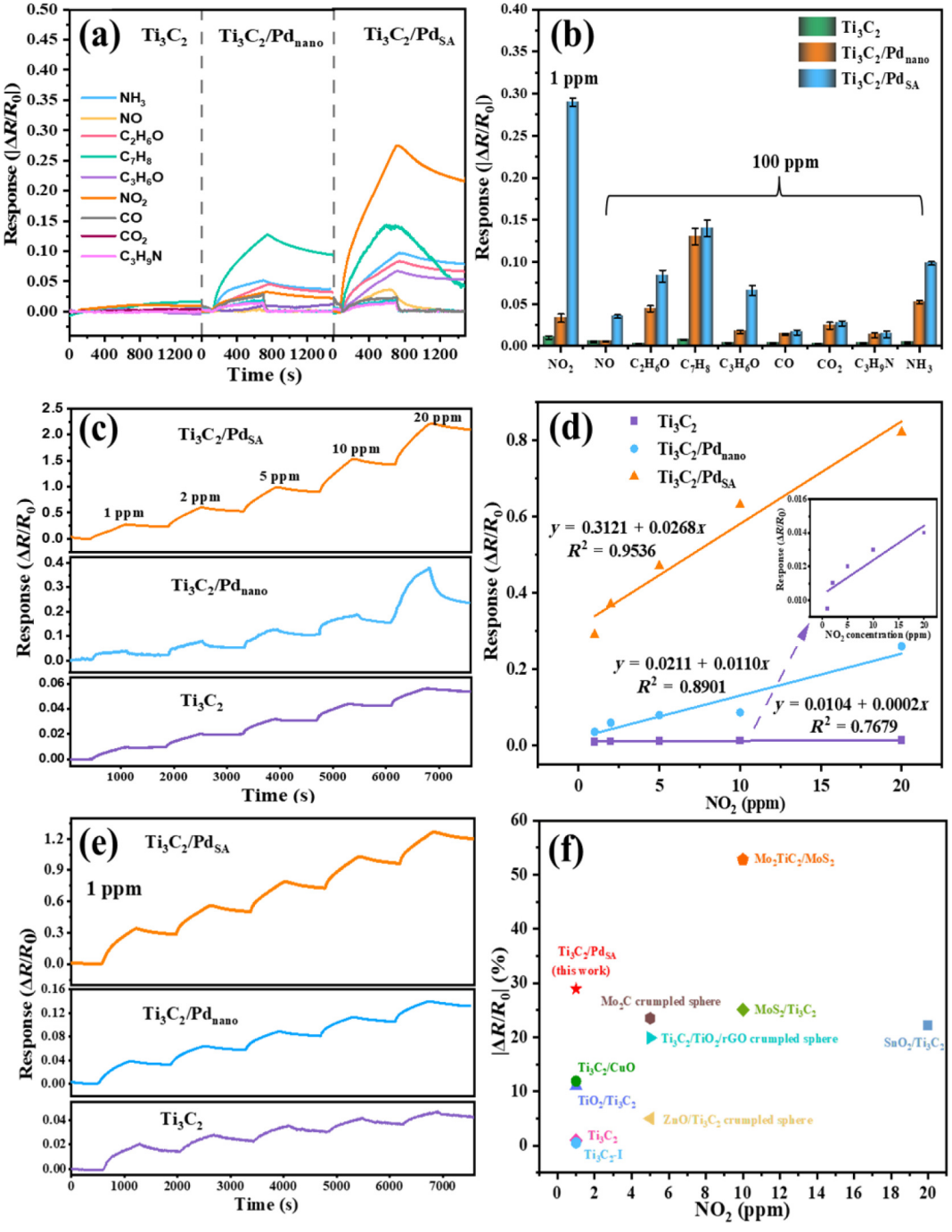

Figure 4 ((a) and (b)) Dynamic response of (a) the sensors toward various analytes at 24 °C and (b) the corresponding calculated response values; ((c) and (d)) dynamic response curves of (c) the sensors toward 1–20 ppm NO_2 at 24 °C and (d) the corresponding liner fitting curves; (e) reproducibility of the sensors at 24 °C; and (f) response values for various state-of-the-art MXene-based NO_2 sensors.

of these three sensors during reproducibility are provided in Fig. S4 in the ESM. The response values of Ti_3C_2/Pd_{SA} and Ti_3C_2/Pd_{nano} were nearly the same, as shown in Fig. 4(b), implying their good repeatability. To examine the stability of Ti_3C_2/Pd_{SA} sensor, this sensor was tested to 1 ppm NO_2 over 14 days, as displayed in Fig. S5 in the ESM. The response value of Ti_3C_2/Pd_{SA} decreased by 8.7% in contrast with the initial value after 14 days, indicating satisfactory long-term stability. Moreover, the response performance of the Ti_3C_2/Pd_{SA} sensor surpassed most recently reported MXenes-based NO_2 sensors operated at room temperature (Fig. 4(f)). The comparison of detailed sensing properties of these NO_2 sensors is summarized in Table S1 in the ESM, demonstrating the superior NO_2 sensing performance of the Ti_3C_2/Pd_{SA} sensor. Ambient humidity is an important aspect that must be examined in practical application. The response of the Ti_3C_2/Pd_{SA} sensor to 1 ppm NO_2 increased from 0.41 to 1.50, with relative humidity (RH) increased from 20% to 80% RH (Fig. S6 in the ESM). The enhancement effect of humidity was attributed to more hydrogen bonds formed between H_2O molecules with NO_2 molecules under a higher humidity environment, which promoted the adsorption of NO_2

and amplified the sensing response [14, 24]. An increase in the humidity enhanced the response of Ti_3C_2/Pd_{SA}, which indicated the potential plications for detecting outdoor NO_2 at room temperature.

3.3 Gas sensing mechanism

The results of the sensing performance investigations have demonstrated that the decoration of Pd atoms effectively boosts the NO_2 sensing properties of Ti_3C_2. To understand the gas sensing mechanism deeply, the activation energy of these three sensors for NO_2 adsorption and desorption was investigated. The activation energy was determined by the following equations [7, 29]

$$R(t) \text{ for } NO_2 \text{ adsorption} = R_{max}\frac{C_aK}{1+C_aK}\left(1-\exp\left(-\frac{1+C_gK}{K}k_{ads}t\right)\right) \quad (3)$$

$$R(t) \text{ for } NO_2 \text{ desorption} = R_0\exp(-k_{des}t) \quad (4)$$

$$k_{ads} \text{ or } k_{des} = A\exp\left(-\frac{E_a}{RT}\right) \quad (5)$$

where k_{ads} and k_{des} are the adsorption and desorption rate constants, K (k_{ads}/k_{des}) is the equilibrium constant, C_a is the concentration of NO_2, R_{max} is the maximum response value, t is the time, C_g is the concentration of NO_2 at time t, R_0 is the response in air, A is a pre-exponential factor, R is the universal gas constant, T is the absolute temperature, and E_a is the activation energy. The k_{ads} and k_{des} of the sensors to 1 ppm NO_2 are calculated by fitting the response versus time curves (Fig. S7 in the ESM) and displayed in Fig. 5(a).

The k_{ads} value of Ti_3C_2/Pd_{SA} sensor (2.25×10^{-3} $ppm^{-1}\cdot s^{-1}$) was approximately 2.37 and 4.19 times higher than those of Ti_3C_2/Pd_{nano} (9.48×10^{-4} $ppm^{-1}\cdot s^{-1}$) and pristine Ti_3C_2 (5.37×10^{-4} $ppm^{-1}\cdot s^{-1}$), respectively. The k_{des} values of Ti_3C_2/Pd_{SA}, Ti_3C_2/Pd_{nano}, and pristine Ti_3C_2 were 3.39×10^{-4}, 5.82×10^{-4}, and 4.19×10^{-4} $ppm^{-1}\cdot s^{-1}$, respectively. The results suggested that Pd atoms obviously promoted the kinetic adsorption of NO_2. To obtain activation energy, the sensing performances of all fabricated sensors to 1 ppm NO_2 at 40 and 60 °C were investigated (Fig. S7 in the ESM). The activation energy of sensing materials was calculated from the slope

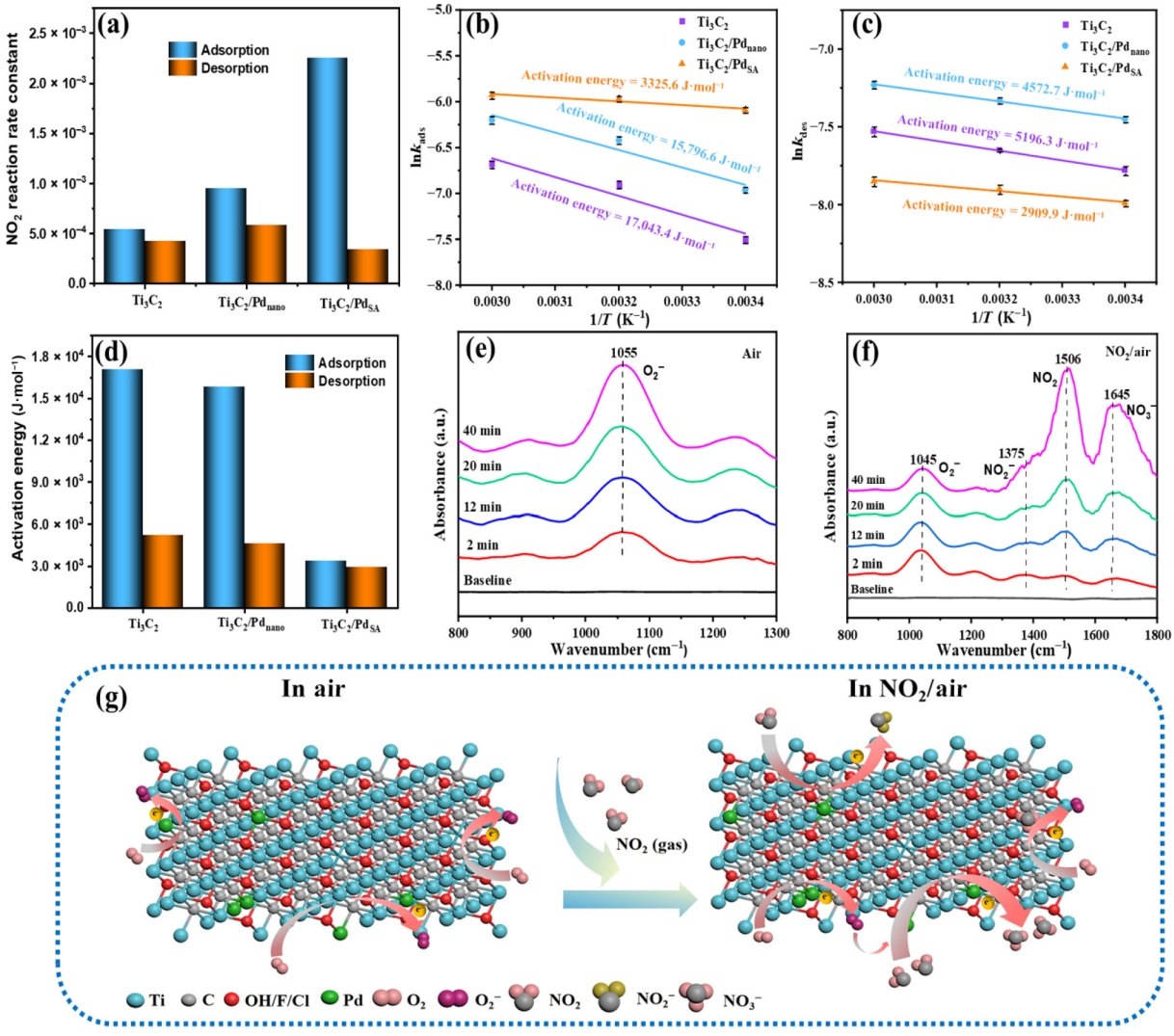

Figure 5 (a) Calculated adsorption (k_{ads}) and desorption (k_{des}) rate constants of the sensors; ((b) and (c)) Arrhenius plots for (b) adsorption and (c) desorption rate constants; (d) calculated activation energy for adsorption and desorption of NO_2 on the sensors; ((e) and (f)) *in-situ* DRIFTS investigation for Ti_3C_2/Pd_{SA} at 24 °C in continuous stream conditions with (e) air (40 min) and then (f) NO_2/air (40 min); and (g) the schematic illustration of Ti_3C_2/Pd_{SA} sensor toward NO_2.

of the plot of $\ln(k_{ads}$ or $k_{des})$ versus $1/T$, as shown in Figs. 5(b)–5(d). For Ti_3C_2/Pd_{SA}, the activation energy obtained for NO_2 adsorption was 3325.6 J·mol^{-1}, which was much less than those of Ti_3C_2/Pd_{nano} (15,796.6 J·mol^{-1}) and pristine Ti_3C_2 (17,043.4 J·mol^{-1}). The activation energy for NO_2 desorption was 2909.9 J·mol^{-1} for Ti_3C_2/Pd_{SA}, whereas 4572.7 J·mol^{-1} for Ti_3C_2/Pd_{nano}, and 5196.3 J·mol^{-1} for pristine Ti_3C_2. These results indicated that Pd atoms can reduce the activation energy of NO_2 adsorption and desorption compared to Ti_3C_2/Pd_{nano} and pristine Ti_3C_2, especially dramatically decreasing the activation energy for NO_2 adsorption.

The *in-situ* DRIFTS was selected to investigate the NO_2 sensing process on the surface of Ti_3C_2/Pd_{SA}. As illustrated in Fig. 5(e), the IR peak that emerged at 1055 cm^{-1} was identified as the absorbed oxygen ion O_2^- [40, 41]. It can be seen that this peak represented O_2^- displayed a pronounced enhancement with the air continued to flow into the reaction chamber. The O_2 molecules were trapped on the surface of the sensing material and turned into O_2^- by capturing free electrons when Ti_3C_2/Pd_{SA} was exposed to air (Reactions (6) and (7)). Figure 5(f) shows the IR peaks changed when the NO_2/air mixed gas was introduced under the same conditions. Some new IR peaks were observed at 1375, 1506, and 1645 cm^{-1}, attributed to NO_2^-, NO_2, and NO_3^- species, respectively [42]. The intensities of these three peaks increased with prolonged reaction time. It was worth noting that the adsorbed NO_2 and the formation NO_3^- species rapidly increased, while the formation NO_2^- species increased slightly. Therefore, the mainly adsorbed NO_2 molecules reacted with O_2^- to form NO_3^- upon Ti_3C_2/Pd_{SA} exposed to NO_2/air (Fig. 5(g)). Meanwhile, some adsorbed NO_2 molecules can directly capture electrons from Ti_3C_2/Pd_{SA} to form NO_2^- (Reactions (8) and (9)). The involved reactions were shown as follows [21, 43]

$$O_2\,(gas) \rightarrow O_2\,(ads) \tag{6}$$

$$O_2\,(ads) + e^- \rightarrow O_2^-\,(ads) \tag{7}$$

$$NO_2\,(gas) + e^- \rightarrow NO_2^-\,(ads) \tag{8}$$

$$2NO_2\,(gas) + O_2^-\,(ads) + e^- \rightarrow 2NO_3^-\,(ads) \tag{9}$$

The O_2 in the air can capture electrons from the Pd, which is beneficial for accelerating the formation of O_2^- at room temperature. Due to the atomically distributed Pd, Ti_3C_2/Pd_{SA} afforded sufficient active sites, and numerous O_2^- participated in the Reaction (9). Therefore, the lower activation energy for NO_2 adsorption and desorption and abundant active sites of Ti_3C_2/Pd_{SA} exhibited excellent sensing properties.

To further clarify the NO_2 sensing mechanism of Ti_3C_2/Pd_{SA}, the DFT simulations with VASP were performed to investigate the adsorption energy and charge transfer between NO_2 and Ti_3C_2/Pd_{SA} surface. Firstly, the adsorption energy of NO_2 molecules on the surface of Ti_3C_2/Pd_{SA}, Ti_3C_2/Pd_{nano}, and Ti_3C_2 was calculated and shown in Fig. 6(a). The three sensing materials corresponding to optimized adsorption structures and the corresponding differential charge density changes are presented in Fig. S8 in the ESM. The adsorption energies were –2.51, –2.04, and –0.24 eV obtained by calculation for Ti_3C_2/Pd_{SA}, Ti_3C_2/Pd_{nano}, and Ti_3C_2, respectively, suggesting the highest adsorption property of Ti_3C_2/Pd_{SA} for NO_2 molecule. Higher adsorption energy indicated a strong interaction between the sensing material and the NO_2 molecule, which enhanced the NO_2 sensing performance. These calculations and DFT analysis were in good agreement with the experimental results.

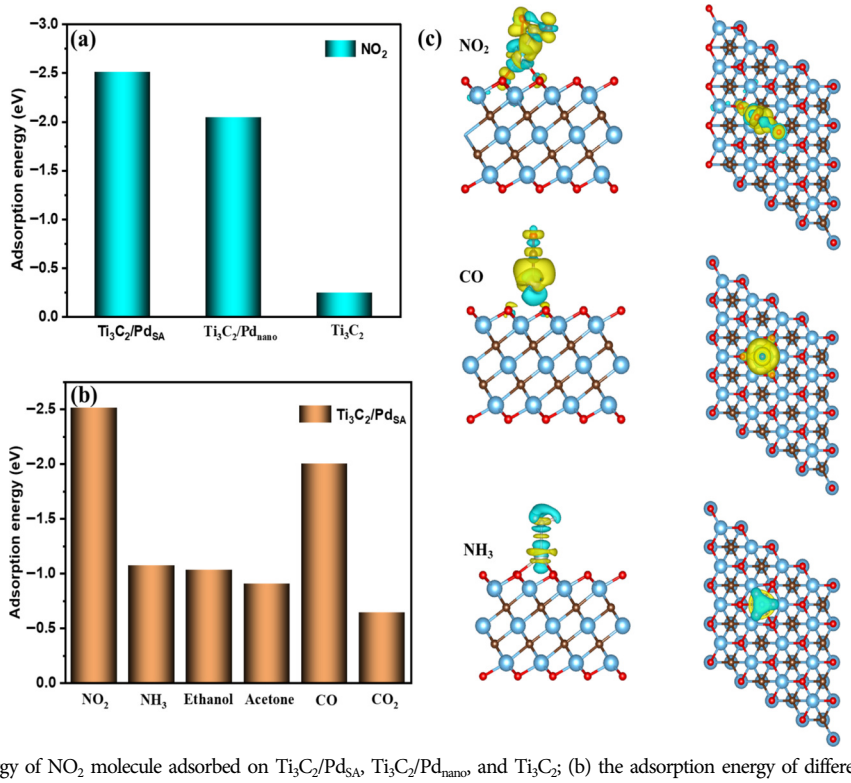

Figure 6 (a) Adsorption energy of NO_2 molecule adsorbed on Ti_3C_2/Pd_{SA}, Ti_3C_2/Pd_{nano}, and Ti_3C_2; (b) the adsorption energy of different gas molecules adsorbed on Ti_3C_2/Pd_{SA}; and (c) charge density difference of NO_2, CO, and NH_3 adsorbed on Ti_3C_2/Pd_{SA}. The yellow and cyan areas correspond to electron accumulation and depletion, respectively (isosurface value of 0.002 e·Å^{-3}).

In addition, the comparison calculation results of NO_2 and other five gas molecules (NH_3, ethanol, acetone, CO, CO_2) adsorption on Ti_3C_2/Pd_{SA} are shown in Fig. 6(b) and Table 1. Among these considered gas molecules, Ti_3C_2/Pd_{SA} displayed the highest adsorption energy (−2.51 eV) and most electron transfer (0.208e) for NO_2 compared with other gas molecules. Figure 6(c) shows the typical differential charge density comparisons of NO_2, CO, and NH_3 adsorption on Ti_3C_2/Pd_{SA}. Meanwhile, the adsorption distance between NO_2 and Ti_3C_2/Pd_{SA} was 1.90 Å, smaller than most other gases. These results demonstrated the excellent NO_2 selectivity of the Ti_3C_2/Pd_{SA} sensor.

Table 1 Adsorption energy, transferred electrons (Δq), the distance between gas molecules, and surface (d) and the doping type of molecule adsorbed on Ti_3C_2/Pd_{SA}

Molecules	E_{ad} (eV)	Δq (e)	d (Å)	Type
NO_2	−2.51	0.208	1.90	Acceptor
NH_3	−1.07	−0.194	2.21	Donor
Ethanol	−1.03	−0.157	2.12	Donor
Acetone	−0.90	−0.100	2.04	Donor
CO	−2.00	0.061	1.85	Acceptor
CO_2	−0.64	0.169	2.09	Acceptor

4 Conclusions

In this work, Ti_3C_2/Pd_{SA} was developed as a sensitive and selective material to detect trace NO_2 gas. The Ti_3C_2/Pd_{SA} was fabricated by direct *in-situ* growth of Pd single atoms on the Ti_3C_2 nanosheet upon taking advantage of rich Ti vacancies and Ti_3C_2 MXene reducing abilities. The introduction of Pd single atoms dramatically enhanced the NO_2 sensing properties of the pristine Ti_3C_2 nanosheet. The Ti_3C_2/Pd_{SA} sensor exhibited a high response value of 0.289 to 1 ppm NO_2, ultralow detection limit (10 ppb), and good selectivity at room temperature. The boosted sensing performance was attributed to abundant active sites, chemical sensitization effect, and gas adsorption enhancement from Pd single atoms in Ti_3C_2/Pd_{SA}. This work provided a prospective avenue for the rational design of high-performance NO_2 gas sensors at room temperature.

Electronic Supplementary Material: Supplementary material (schematic diagram of measurement system, additional SEM images, the detection limit, the impact of RH, fitting curves of dynamic response, and NO_2 sensing performance comparison table) is available in the online version of this article at https://doi.org/10.26599/NR.2025.94907285.

Data availability

All data needed to support the conclusions in the paper are presented in the manuscript and the Electronic Supplementary Material. Additional data related to this paper may be requested from the corresponding author upon request.

Acknowledgements

This work was financially supported by Guangdong Basic and Applied Basic Research Foundation (No. 2023A1515140020), the National Natural Science Foundation of China (Nos. 52070042 and 52300127), and Characteristic Innovation Project of Guangdong Universities (No. 2024KTSCX213).

Declaration of competing interest

All the contributing authors report no conflict of interests in this work.

Author contribution statement

Y. C.: Conceptualization, methodology, investigation, formal analysis, writing – original draft. J. L. X.: Investigation, methodology. Y. W. W.: Formal analysis, methodology. H. M. A. S.: Formal analysis. J. H. C.: Investigation. T. P.: Methodology. X. R. T.: Investigation, software. Z. L.: Supervision. C. P. L.: Writing – review & editing, resources, funding acquisition. All the authors have approved the final manuscript.

Use of AI statement

None.

References

[1] Lim, H.; Kwon, H.; Kang, H.; Jang, J. E.; Kwon, H. J. Semiconducting MOFs on ultraviolet laser-induced graphene with a hierarchical pore architecture for NO_2 monitoring. *Nat. Commun.* **2023**, *14*, 3114.

[2] Song, J.; Baek, J.; Cho, J.; Kim, T.; Kim, M.; Kim, H. S.; Mun, J.; Kang, S. W. MOCVD of hierarchical C-MoS_2 nanobranches for ppt-level NO_2 detection. *Small Struct.* **2023**, *4*, 2200392.

[3] Choi, J.; Kim, Y. J.; Cho, S. Y.; Park, K.; Kang, H.; Kim, S. J.; Jung, H. T. *In situ* formation of multiple schottky barriers in a Ti_3C_2 MXene film and its application in highly sensitive gas sensors. *Adv. Funct. Mater.* **2020**, *30*, 2003998.

[4] Wu, J.; Wu, Z. X.; Ding, H. J.; Wei, Y. M.; Huang, W. X.; Yang, X.; Li, Z. Y.; Qiu, L.; Wang, X. T. Three-dimensional graphene hydrogel decorated with SnO_2 for high-performance NO_2 sensing with enhanced immunity to humidity. *ACS Appl. Mater. Interfaces* **2020**, *12*, 2634–2643.

[5] Zheng, L.; Wang, X. W.; Jiang, H. J.; Xu, M. Z.; Huang, W.; Liu, Z. Recent progress of flexible electronics by 2D transition metal dichalcogenides. *Nano Res.* **2022**, *15*, 2413–2432.

[6] Panigrahi, P.; Hussain, T.; Karton, A.; Ahuja, R. Elemental substitution of two-dimensional transition metal dichalcogenides ($MoSe_2$ and $MoTe_2$): Implications for enhanced gas sensing. *ACS Sens.* **2019**, *4*, 2646–2653.

[7] Koo, W. T.; Kim, S. J.; Jang, J. S.; Kim, D. H.; Kim, I. D. Catalytic metal nanoparticles embedded in conductive metal-organic frameworks for chemiresistors: Highly active and conductive porous materials. *Adv. Sci.* **2019**, *6*, 1900250.

[8] Lin, C. X.; Kim, K.; Wang, Z. C.; Yan, Z.; Tang, Z. Y.; Liu, Y. L. Mace-like TTF-TCNQ/HKUST-1 composite structures for rapid NO_2 detection: Synergistically induced ultrahigh sensitivity and outstanding selectivity. *Nano Res.* **2023**, *16*, 13366–13374.

[9] Sreedhar, A.; Ravi, P.; Noh, J. S. Advancements in two-dimensional Ti_3C_2 MXene interfaced semiconductors for room temperature NO_2 gas sensing: A review. *J. Mater. Sci. Technol.* **2024**, *203*, 237–254.

[10] Li, H. P.; Wen, J.; Ding, S. M.; Ding, J. B.; Song, Z. H.; Zhang, C.; Ge, Z.; Liu, X.; Zhao, R. Z.; Li, F. C. Synergistic coupling of 0D–2D heterostructure from ZnO and $Ti_3C_2T_x$ MXene-derived TiO_2 for boosted NO_2 detection at room temperature. *Nano Mater. Sci.* **2023**, *5*, 421–428.

[11] Hilal, M.; Yang, W.; Hwang, Y.; Xie, W. F. Tailoring MXene

thickness and functionalization for enhanced room-temperature trace NO_2 sensing. *Nano-Micro Lett.* **2024**, *16*, 84.
[12] Guo, F. Q.; Feng, C.; Zhang, Z.; Zhang, L. L.; Xu, C.; Zhang, C. T.; Lin, S.; Wu, H. X.; Zhang, B. H.; Tabusi, A. et al. A room-temperature NO_2 sensor based on $Ti_3C_2T_X$ MXene modified with sphere-like CuO. *Sens. Actuators B: Chem.* **2023**, *375*, 132885.
[13] Wang, B.; Gao, X. X.; He, J. M.; Xiao, Y. N.; Liu, Y.; Jia, X. T.; Zhang, K.; Wang, C. G.; Sun, P.; Liu, F. M. et al. Room-temperature ppb-level NO_2 sensor based on three-dimensional Mo_2CT_x nano-crumpled spheres. *Sens. Actuators B: Chem.* **2024**, *399*, 134790.
[14] Zhao, Q. N.; Zhou, W. Z.; Zhang, M. X.; Wang, Y.; Duan, Z. H.; Tan, C. L.; Liu, B. H.; Ouyang, F. P.; Yuan, Z.; Tai, H. L. et al. Edge-enriched $Mo_2TiC_2T_x/MoS_2$ heterostructure with coupling interface for selective NO_2 monitoring. *Adv. Funct. Mater.* **2022**, *32*, 2203528.
[15] Ta, Q. T. H.; Tri, N. N.; Noh, J. S. Improved NO_2 gas sensing performance of 2D $MoS_2/Ti_3C_2T_x$ MXene nanocomposite. *Appl. Surf. Sci.* **2022**, *604*, 154624.
[16] Chen, W. M.; Li, P. P.; Yu, J.; Cui, P. X.; Yu, X. H.; Song, W. G.; Cao, C. Y. *In-situ* doping nickel single atoms in two-dimensional MXenes analogue support for room temperature NO_2 sensing. *Nano Res.* **2022**, *15*, 9544–9553.
[17] Kuang, D. L.; Wang, L.; Guo, X. Z.; She, Y.; Du, B. S.; Liang, C. Y.; Qu, W. J.; Sun, X.; Wu, Z. L.; Hu, W. et al. Facile hydrothermal synthesis of $Ti_3C_2T_x$-TiO_2 nanocomposites for gaseous volatile organic compounds detection at room temperature. *J. Hazard. Mater.* **2021**, *416*, 126171.
[18] Yang, Z. J.; Zou, H. S.; Zhang, Y. Y.; Liu, F. M.; Wang, J.; Lv, S. Y.; Jiang, L.; Wang, C. G.; Yan, X.; Sun, P. et al. The introduction of defects in $Ti_3C_2T_x$ and $Ti_3C_2T_x$-assisted reduction of graphene oxide for highly selective detection of ppb-level NO_2. *Adv. Funct. Mater.* **2022**, *32*, 2108959.
[19] Gasso, S.; Sohal, M. K.; Mahajan, A. MXene modulated SnO_2 gas sensor for ultra-responsive room-temperature detection of NO_2. *Sens. Actuators B: Chem.* **2022**, *357*, 131427.
[20] Liu, X.; Zhang, H. M.; Shen, T.; Sun, J. B. Flexible resistive NO_2 gas sensor of $SnO_2@Ti_3C_2T_x$ MXene for room temperature application. *Ceram. Int.* **2024**, *50*, 2459–2466.
[21] Yang, Z. J.; Jiang, L.; Wang, J.; Liu, F. M.; He, J. M.; Liu, A.; Lv, S. Y.; You, R.; Yan, X.; Sun, P. et al. Flexible resistive NO_2 gas sensor of three-dimensional crumpled MXene $Ti_3C_2T_x$/ZnO spheres for room temperature application. *Sens. Actuators B: Chem.* **2021**, *326*, 128828.
[22] Nam, M. S.; Kim, J. Y.; Mirzaei, A.; Lee, M. H.; Kim, H. W.; Kim, S. S. Au-and Pt-decorated $Ti_3C_2T_x$ MXenes for preparing self-heated and flexible NH_3 gas sensors. *Sens. Actuators B: Chem.* **2024**, *403*, 135112.
[23] Zong, B. Y.; Xu, Q. K.; Mao, S. Single-atom Pt-functionalized $Ti_3C_2T_x$ field-effect transistor for volatile organic compound gas detection. *ACS Sens.* **2022**, *7*, 1874–1882.
[24] Hu, J. Y.; Wang, X. P.; Lei, H.; Luo, M. H.; Zhang, Y. Plasmonic photothermal driven MXene-based gas sensor for highly sensitive NO_2 detection at room temperature. *Sens. Actuators B: Chem.* **2024**, *407*, 135422.
[25] Liang, X.; Fu, N. H.; Yao, S. C.; Li, Z.; Li, Y. D. The progress and outlook of metal single-atom-site catalysis. *J. Am. Chem. Soc.* **2022**, *144*, 18155–18174.
[26] Wang, W. Y.; Li, S. J.; Qiang, Q.; Wu, K.; Pan, X. L.; Su, W. T.; Cai, J. Y.; Shen, Z. G.; Yang, Y. Q.; Li, C. Z. et al. Catalytic refining lignin-derived monomers: Seesaw effect between nanoparticle and single-atom Pt. *Angew. Chem., Int. Ed.* **2024**, *63*, e202404683.
[27] Chen, C.; Ou, W.; Yam, K. M.; Xi, S. B.; Zhao, X. X.; Chen, S.; Li, J.; Lyu, P.; Ma, L.; Du, Y. H. et al. Zero-valent palladium single-atoms catalysts confined in black phosphorus for efficient semi-hydrogenation. *Adv. Mater.* **2021**, *33*, 2008471.
[28] Chu, T. S.; Rong, C.; Zhou, L.; Mao, X. Y.; Zhang, B. W.; Xuan, F. Z. Progress and perspectives of single-atom catalysts for gas sensing. *Adv. Mater.* **2023**, *35*, 2206783.
[29] Jia, X.; Qiao, P. Z.; Wang, X. W.; Yan, M. Y.; Chen, Y.; An, B. L.; Hu, P. F.; Lu, B.; Xu, J.; Xue, Z. G. et al. Building feedback-regulation system through atomic design for highly active SO_2 sensing. *Nano-Micro Lett.* **2024**, *16*, 136.
[30] Zhang, S. C.; Chang, X.; Zhou, L. H.; Liu, X. H.; Zhang, J. Stabilizing single-atom Pt on Fe_2O_3 nanosheets by constructing oxygen vacancies for ultrafast H_2 sensing. *ACS Sens.* **2024**, *9*, 2101–2109.
[31] Wang, C. Y.; Xie, J. Y.; Chang, X.; Zheng, W.; Zhang, J.; Liu, X. H. ZnO single nanowire gas sensor: A platform to investigate the sensitization of Pt. *Chem. Eng. J.* **2023**, *473*, 145481.
[32] Ye, X. L.; Lin, S. J.; Zhang, J. W.; Jiang, H. J.; Cao, L. A.; Wen, Y. Y.; Yao, M. S.; Li, W. H.; Wang, G. E.; Xu, G. Boosting room temperature sensing performances by atomically dispersed Pd stabilized via surface coordination. *ACS Sens.* **2021**, *6*, 1103–1110.
[33] Xue, Z. G.; Yan, M. Y.; Yu, X.; Tong, Y. J.; Zhou, H.; Zhao, Y. F.; Wang, Z. Y.; Zhang, Y. S.; Xiong, C.; Yang, J. et al. One-dimensional segregated single Au sites on step-rich ZnO ladder for ultrasensitive NO_2 sensors. *Chem* **2020**, *6*, 3364–3373.
[34] Zhu, L. Y.; Ou, L. X.; Mao, L. W.; Wu, X. Y.; Liu, Y. P.; Lu, H. L. Advances in noble metal-decorated metal oxide nanomaterials for chemiresistive gas sensors: Overview. *Nano-Micro Lett.* **2023**, *15*, 89.
[35] Xiong, J. L.; Cai, Y.; Nie, X. L.; Wang, Y. W.; Song, H. R.; Sharif, H. M. A.; Li, Z.; Li, C. P. PANI/3D crumpled $Ti_3C_2T_X/TiO_2$ nanocomposites for flexible conductometric NH_3 sensors working at room temperature. *Sens. Actuators B: Chem.* **2023**, *390*, 133987.
[36] Zhao, D.; Chen, Z.; Yang, W. J.; Liu, S. J.; Zhang, X.; Yu, Y.; Cheong, W. C.; Zheng, L. R.; Ren, F. Q.; Ying, G. B. et al. MXene (Ti_3C_2) vacancy-confined single-atom catalyst for efficient functionalization of CO_2. *J. Am. Chem. Soc.* **2019**, *141*, 4086–4093.
[37] Xiu, L. Y.; Wang, Z. Y.; Yu, M. Z.; Wu, X. H.; Qiu, J. S. Aggregation-resistant 3D MXene-based architecture as efficient bifunctional electrocatalyst for overall water splitting. *ACS Nano* **2018**, *12*, 8017–8028.
[38] Zhou, S. Q.; Shang, L.; Zhao, Y. X.; Shi, R.; Waterhouse, G. I. N.; Huang, Y. C.; Zheng, L. R.; Zhang, T. R. Pd single-atom catalysts on nitrogen-doped graphene for the highly selective photothermal hydrogenation of acetylene to ethylene. *Adv. Mater.* **2019**, *31*, 1900509.
[39] Lv, D. W.; Shen, W. F.; Chen, W. G.; Tan, R. Q.; Xu, L.; Song, W. J. PSS-PANI/PVDF composite based flexible NH_3 sensors with sub-ppm detection at room temperature. *Sens. Actuators B: Chem.* **2021**, *328*, 129085.
[40] Li, J. Y.; Si, W. Z.; Shi, L.; Gao, R. Q.; Li, Q. J.; An, W.; Zhao, Z. C.; Zhang, L.; Bai, N.; Zou, X. X. et al. Essential role of lattice oxygen in hydrogen sensing reaction. *Nat. Commun.* **2024**, *15*, 2998.
[41] Lou, C. M.; Wang, K.; Liu, X. H.; Li, X. Y.; Wang, H.; Li, L. H.; Zheng, W.; Zhang, J. Heterogeneous Co_3O_4/carbon nanofibers for low temperature triethylamine detection: Mechanistic insights by *operando* DRIFTS and DFT. *Adv. Mater. Interfaces* **2022**, *9*, 2101479.
[42] Tang, H. Y.; Luo, X. A.; Li, W. T.; Pan, Y.; Wang, S. Q.; Ma, H.; Shen, Y.; Fang, R. M.; Dong, F. Highly active Ag/ZnO/ZnAl-LDH heterojunction photocatalysts for NO removal. *Chem. Eng. J.* **2023**, *474*, 145873.
[43] Bai, H. N.; Guo, H.; Feng, C.; Wang, J.; Liu, B.; Xie, Z. L.; Guo, F. Q.; Chen, D. J.; Zhang, R.; Zheng, Y. D. Highly responsive and selective ppb-level NO_2 gas sensor based on porous Pd-functionalized CuO/rGO at room temperature. *J. Mater. Chem. C* **2022**, *10*, 3756–3769.